

Evolution and afterglow emission of gamma-ray burst jets from binary neutron star mergers

E. Dreas^{1,2,3,★}, O. S. Salafia^{4,5}, A. Pavan^{2,6}, R. Ciolfi^{2,6}, and A. Celotti^{1,3,4,7}

¹ SISSA, Via Bonomea 265, I-34136 Trieste, Italy

² INAF, Osservatorio Astronomico di Padova, Vicolo dell’Osservatorio 5, I-35127 Padova, Italy

³ INFN, Sezione di Trieste, Via Valerio 2, I-34127 Trieste, Italy

⁴ INAF, Osservatorio Astronomico di Brera, via Bianchi 46, I-23807 Merate, Italy

⁵ INFN, Sezione di Milano-Bicocca, Piazza della Scienza 3, I-20126 Milano, Italy

⁶ INFN, Sezione di Padova, Via Francesco Marzolo 8, I-35131 Padova, Italy

⁷ IFPU, Via Beirut 2, I-34151 Trieste, Italy

Received xxx; accepted xxx

ABSTRACT

Context. Relativistic jets launched in binary neutron star (BNS) mergers are widely accepted as the engines powering most of the population of short gamma-ray bursts (GRBs). Understanding their structure and dynamics—particularly during and after breakout from the merger ejecta—is crucial for interpreting GRB afterglows, especially for off-axis observers. Traditional models often assume simple angular or radial jet profiles, potentially missing key features emerging for jets piercing through realistic environments.

Aims. This work aims to investigate the formation and evolution of the jet structure as it propagates through a non-homogeneous, anisotropic BNS merger environment. We focus on how the interaction with the ambient medium shapes the jet’s angular and velocity distributions and assess the impact of this realistic structure on the resulting afterglow light curves.

Methods. We perform a series of 3D relativistic magnetohydrodynamic simulations of jets launched in post-merger environments, exploring different injection conditions. Simulations are evolved to late times, approaching the ballistic regime, where further dynamical evolution becomes negligible. From the resulting outflows, we extract energy and velocity profiles and compute multi-wavelength afterglow light curves using a semi-analytic model that includes radial stratification and the full 3D jet geometry.

Results. More energetic or earlier-launched jets drill more efficiently through the ejecta, but all develop asymmetries that leave clear imprints in the off-axis afterglow light curves. All models exhibit a complex multi-shock breakout structure responsible for an early, dimmer peak in the afterglow. Despite structural differences, all simulated jets are consistent with the observational data of the multi-messenger BNS merger event GW170817.

Key words. magnetohydrodynamics (MHD) – gamma-ray burst: general – stars: jets – relativistic processes – methods: numerical

1. Introduction

Gamma-ray bursts (GRBs) are the most energetic explosions in the universe, observed as brief flashes of gamma rays followed by longer-lasting broadband afterglow emission. They are believed to originate from two main types of progenitors: the collapse of massive stars and the mergers of compact binary systems involving neutron stars or black holes (Eichler et al. 1989; Narayan et al. 1992; Woosley 1993; Berger 2014). The multi-messenger detection of GW170817 and its associated GRB 170817A prompted extensive multi-wavelength observations of a GRB originating from a binary neutron star merger (Abbott et al. 2017b,c,a), offering a detailed view of the afterglow evolution and confirming that these systems can launch highly relativistic, collimated outflows (Mooley et al. 2018a; Ghirlanda et al. 2019). In this work, we focus on GRBs arising from binary neutron star (BNS) mergers.

Numerical simulations – especially those using relativistic magnetohydrodynamics (RMHD) – can offer a realistic treatment of the jet launching and early evolution, incorporating magnetic fields, collimation shocks, and time-dependent energy injection from the central engine (e.g. Komissarov et al. 2009;

Tchekhovskoy et al. 2010; Gottlieb et al. 2023). The afterglow emission is produced when the relativistic ejecta interact with the ‘circum-burst’ medium surrounding the progenitor, generating shocks that accelerate electrons and amplify magnetic fields, resulting in synchrotron emission observable across the electromagnetic spectrum (Mészáros & Rees 1997; Sari et al. 1998). Modelling this afterglow emission is crucial for interpreting observed light curves and spectra, as well as for constraining key physical parameters such as the jet energy, circum-burst density, and angular structure of the outflow (see e.g. Nakar 2020; Granot & van der Horst 2014).

While analytic and semi-analytic afterglow analyses have successfully captured many observational features, they often rely on idealised assumptions and simplified jet structures, which may not accurately reflect the physical properties of the jet material. Indeed, there remains a disconnection between the early-time evolution modelled in RMHD simulations and the late-time behaviour of the outflow, where the jet becomes kinetically dominated and asymptotically approaches a ballistic expansion regime. Bridging this gap requires robust methods for extracting the physical state of the jet from simulations and evolving it up to where radiative processes become observable.

* edreas@sissa.it

Here, we present a framework to model the afterglow emission of GRB jets using the data extracted from RMHD simulations, with a particular focus on the transition to ballistic expansion, following the work presented in Dreas et al. 2025. Our approach integrates RMHD simulation outputs with semi-analytic hydrodynamical and radiative calculations, enabling a consistent mapping from the simulation domain to synthetic afterglow observables. We aim at quantifying how the features imprinted during the RMHD-dominated phase affect the observed light curves and viewing angle dependence, and how these features are affected by different jet injection parameters.

This work builds on recent efforts to incorporate simulation-informed jet structures into afterglow models (e.g. Gottlieb et al. 2017; Lazzati et al. 2018; Gill et al. 2019; Kathirgamaraju et al. 2019; Nativi et al. 2021, 2022; Gottlieb et al. 2022). Our approach considers the evolution of relativistic jets within a realistic, non-homogeneous BNS merger environment (Ciolfi 2020, Pavan et al. 2021, 2023, Pais et al. 2024), capturing the complexity of the resulting jet-ambient medium interaction.

By continuing the simulation into the ballistic regime, we capture the full transition from jet breakout to free expansion, ensuring that the jet structure used for afterglow predictions reflects its final dynamical state. The resulting 3D energy and velocity distributions are then used as input to compute afterglow emission in the framework of the external shock model, where the decelerating jet interacts with the interstellar medium.

In this context, the radial stratification of the outflow – i.e., the distribution of energy across shells with different Lorentz factors – plays a critical role in shaping the light curve (e.g. Panaiteanu et al. 1998; Sari & Mészáros 2000; Zhang et al. 2006; Lamb et al. 2020; Fraija et al. 2022; Moss et al. 2023). As slower-moving shells catch up with the decelerating shock front, they inject additional energy into the blast wave, modifying the afterglow dynamics. This energy injection process affects both the timing and morphology of the afterglow rise, and can introduce characteristic features such as shallow rises or plateaus, especially for off-axis observers.

The paper is structured as follows. In Section 2, we present the simulation setup, the various jet models and the different results in terms of dynamical evolution and energetics. In Section 3, we analyse the angular distribution of the jet material and compare the different resulting structures. In Section 4, we use such jet structures to compute the afterglow light curves with an enhanced afterglow model. Finally, in Section 5 we discuss our results.

2. Impact of injection parameters on jet evolution

Pavan et al. 2025 (hereafter P25) investigated how varying injection parameters – namely the jet’s initial luminosity, decay time scale, magnetisation, and launching time – affect the evolution of a jet propagating through a realistic post-merger environment, i.e. directly imported from a BNS merger simulation (Ciolfi 2020). Here, we summarise the key outcomes during the first three seconds of evolution, as reported in P25, and extend the analysis by following the jet dynamics up to nine seconds.

2.1. Numerical setup

All simulations are performed using the RMHD module of the PLUTO code (Mignone et al. 2007). The first three seconds of evolution following the jet launching time, t_j , are reproduced on a 3D spherical computational grid, as detailed in P25. Then, at

$t - t_j = 3$ s, the simulation is transferred to a Cartesian grid using the remapping procedure outlined in Dreas et al. 2025 (hereafter D25), which enables the evolution to be followed up to $t_{\text{end}} \equiv t - t_j = 9$ s without loss of resolution. In particular, we focus on the evolution of the northern side of the jet, as in D25, though the same procedure can be equally applied to the southern side.

Specifically, the Cartesian grid spans $x, z \in [-2.33, +2.33] \times 10^6$ km and $y \in [0.3, 6.3] \times 10^6$ km, with the y -axis being aligned to the main jet propagation direction. The grid resolution is uniform along all axes, with $656 \times 864 \times 656$ points along the x -, y - and z -axes, respectively. Numerical integration is carried out employing piecewise parabolic reconstruction, the HLL Riemann solver, third-order Runge–Kutta time stepping, and hyperbolic divergence cleaning to enforce $\nabla \cdot \mathbf{B} = 0$ (Mignone & Tzeferacos 2010; Mignone et al. 2010). Furthermore, a Taub-Matthews equation of state (TM EOS hereafter) is adopted to relate thermodynamic quantities (Mignone et al. 2005, Mignone & McKinney 2007).

Below, we discuss the results of our simulations for the various jet models considered, whose injection parameters and properties at t_{end} are summarised in Table 1.

2.2. Fiducial model

Our fiducial model F , used as the baseline for varying injection parameters in the other models, describes the evolution of a manually injected jet at $t_j = 385$ ms after merger, with an initial luminosity of $L_j = 5.37 \times 10^{51}$ erg/s, exponentially decaying with a time scale of $\tau_d = 300$ ms, and magnetic field contribution to the total injected luminosity of $\Sigma_j = 1.2\%$ (see Section 2.1 in P25).

Figure 1 shows the configuration of the jet-environment system for the fiducial model, in the meridional plane at three key stages: at 275 ms after launch (lower panel), at the end of the first three seconds of evolution within the spherical grid, and at t_{end} (upper panels).

In this model, the jet’s evolution is characterised by intense mixing with the realistic BNS merger environment. At $t_j \approx 275$ ms the jet and cocoon, regions (1) and (2) in Fig. 1, pierce through the inner merger environment, region (3). We refer to this moment as the breakout time (see the lower panels in the Figure). Before the breakout, approximately half of the injected energy is deposited into the inner environment (see Table 2 in P25). Following breakout, the jet head undergoes a sharp transition as it emerges from the dense environment and begins accelerating into a much lower-density medium. The distribution of the corresponding energy density, without the rest mass component (e_{sum} , left column), reveals an isotropic bubble of non-negligible energy, corresponding to the dynamical ejecta imported from the merger simulation. We refer to this region as the outer merger environment (indicated in the Figure as region 4). At approximately 3 s after launch, the jet head reaches the boundary of the outer merger environment, having accelerated up to a maximum Lorentz factor of ≈ 56 .

The jet ejecta propagation within the atmosphere (region 5), after $t - t_j = 3$ s, is followed in the uniform Cartesian grid (see Section 2.1). As the evolution proceeds, the system enters a phase of homologous expansion, during which the shocked material settles into a multi-component, stratified structure. Specifically, we identify the *jet cap*, region (6) in the Figure, as the zone containing most of the jet energy. The jet cap is formally defined as the radial extent where the kinetic energy flux is above 15% of its maximum¹. Note that in our previous works we referred to

¹ See P25 and refs. therein.

Table 1: Jet injection parameters and main properties at t_{end} for all jet models.

Model	Injection parameters				Properties at $t_{\text{end}} = 9$ s				
	t_{j} [ms]	L_{j} [erg/s]	τ_{d} [ms]	Σ_{j}	$E_{\text{iso,max}}$ [erg]	$\bar{\Gamma}_{\text{max}} _{\Phi_{\text{avg}}}$	$E_{\text{kin}}/E_{\text{sum}}$	Θ_{50} [$^{\circ}$]	Θ_{off} [$^{\circ}$]
<i>F</i>	385	5.37×10^{51}	300	1.20%	1.46×10^{53}	27.7	0.97	5.6	1.4
<i>a</i> ($L_{\text{j}} \uparrow$)	385	8.95×10^{51}	300	1.20%	4.57×10^{53}	40.7	0.97	5.1	1.6
<i>b</i> ($\tau_{\text{d}} \uparrow$)	385	5.37×10^{51}	500	1.20%	3.93×10^{53}	80.1	0.95	4.9	1
<i>c</i> ($B_{\text{j}} \uparrow$)	385	5.37×10^{51}	300	1.56%	1.94×10^{53}	26.8	0.97	5.0	2.7
<i>d</i> ($B_{\text{j}} \uparrow, L_{\text{j}} \downarrow$)	385	4.12×10^{51}	300	1.56%	1.26×10^{53}	34.2	0.96	5.2	1.5
<i>e1</i> ($B_{\text{j}} \downarrow, L_{\text{j}} \downarrow$)	385	3.69×10^{51}	300	0.46%	0.97×10^{53}	23.6	0.96	6.1	3.6
<i>e2</i> ($B_{\text{j}} \downarrow, L_{\text{j}} \downarrow, t_{\text{j}} \downarrow$)	185	3.69×10^{51}	300	0.46%	2.33×10^{53}	54.1	0.97	4.6	0.9

Notes. The injection parameters considered in the study are the jet launching time (with respect to merger) t_{j} , injected luminosity L_{j} , decay time scale of the injected luminosity τ_{d} , and relative contribution of the magnetic field to the total luminosity Σ_{j} . The table also shows, for each model, some properties of the jet cap (see text for definitions) at the end of the extended simulation, namely the maximum isotropic equivalent energy $E_{\text{iso,max}}$, the maximum of the radially- and azimuthally-averaged Lorentz factor $\bar{\Gamma}_{\text{max}}|_{\Phi_{\text{avg}}}$, the ratio of kinetic over total (excluding rest mass) energy $E_{\text{kin}}/E_{\text{sum}}$, the effective half-opening angle Θ_{50} , and the offset of the jet barycentre with respect to the injection axis Θ_{off} . The parameters shown next to each model label denote deviations (increases or decreases) from the fiducial model *F*.

this region as the ‘jet head’: here we update the terminology to avoid confusion with its canonical definition. The jet cap is preceded by a thin shell of shocked material, region (7), to which we will refer as *outer shell* (see Section 2.7 for further discussion).

During this phase, the jet ejecta undergo residual conversion of the retained thermo-magnetic energy into kinetic form, along with the development of a stable angular structure (see further discussion in Section 2.6).

2.3. Influence of luminosity and decay time scale

Models *a* and *b* represent more energetic jets compared to the fiducial case. Specifically, model *a* features an initial luminosity that is $\approx 170\%$ of that of model *F*, while model *b* has the same jet luminosity as the fiducial case, but features a longer injection time scale $\tau_{\text{d}} = 500$ ms, reaching the same total injected energy as model *a* over the full simulation time span.

As a result of its higher L_{j} , model *a* exhibits faster jet propagation than the other models, achieving breakout at $t_{\text{j}} \approx 200$ ms. Model *b* follows a similar early-time evolution and breakout time as the fiducial model, but drills more efficiently through the same inner merger environment. Notably, both models *a* and *b* retain a larger fraction ($\approx 60\%$) of injected energy at the jet cap compared to model *F*. This enhances jet acceleration into the outer merger environment, resulting in local maximum Lorentz factors of 85 and 102 in models *a* and *b*, respectively, at $t - t_{\text{j}} = 3$ s.

2.4. Influence of magnetisation

Models *c* and *d* feature an increased magnetic field contribution ($\Sigma_{\text{j}} = 1.56\%$) with respect to model *F*. Additionally, model *d* employs a lower initial luminosity ($\approx 75\%$ with respect to the fiducial) to assess the impact of magnetisation relative to jet power (see Table 1).

In both models, the higher initial jet magnetisation is associated with better preservation of the jet’s toroidal magnetic field, owing to the suppression of hydrodynamical instabilities at the jet-environment interface (see Figures 6 and 7 of P25). This, in turn, results in higher jet collimation throughout propagation, despite the same (or even lower) initial jet luminosity relative to the fiducial case (further discussion in Section 3). On the other hand, the jet dynamics and energetics remain similar between models *c* and *F*, whereas the reduced L_{j} in model *d* leads to a less efficient jet drilling, resulting in a slightly longer breakout time

($t_{\text{j}} \approx 300$ ms) and increased energy deposition into the surrounding environment (see P25).

2.5. Influence of launching time

Finally, the impact of jet launching time is examined by considering two models with identical injection properties – both with lower initial luminosity and magnetisation compared to the fiducial model, see Table 1 – but different injection times, $t_{\text{j}} = 385$ ms and 185 ms after merger for model *e1* and *e2*, respectively.

As expected, t_{j} has a significant impact on both the mass and radial extent of the merger environment that the jet needs to drill through. Specifically, in model *e1*, the surrounding medium is approximately a factor 2 more massive and extends about 4 times farther at the time of jet launch than in model *e2*. For the low-luminosity, low-magnetisation model *e1*, the jet undergoes severe disruption as it interacts with the merger environment, with more than half of the injected energy being deposited into the environment itself and a final jet angular structure that lacks a well-defined ultra-relativistic core (Section 3).

In contrast, model *e2* encounters a much less extended and less massive medium, reducing both the strength and duration of the jet–environment interaction. Notably, the jet breaks out in just 100 ms (the fastest among all models), while retaining over half of the injected energy at the jet cap. In addition, the jet retains a collimated angular structure with an ultra-relativistic core and a toroidally dominated magnetic field configuration (see Figure 8 of P25). These results highlight that the jet launching time plays a major role in determining the outcome of propagation (whether the incipient jet successfully breaks out or becomes choked) in realistic BNS merger environments (see, e.g., Murguia-Berthier et al. 2014, Lyutikov 2020 and Pais et al. 2024 for previous analyses on the jet choking conditions).

2.6. Energy budget and ballistic regime

In this Section, we summarise the evolution of the energy budget across the various models and describe the onset of the ballistic (or coasting) regime, which marks the point where the jet can be considered dynamically stable for afterglow modelling. Note that, unless stated otherwise, the values of energy discussed in this Section are referred to the whole system, intended as jet, cocoon, inner and outer merger environment.

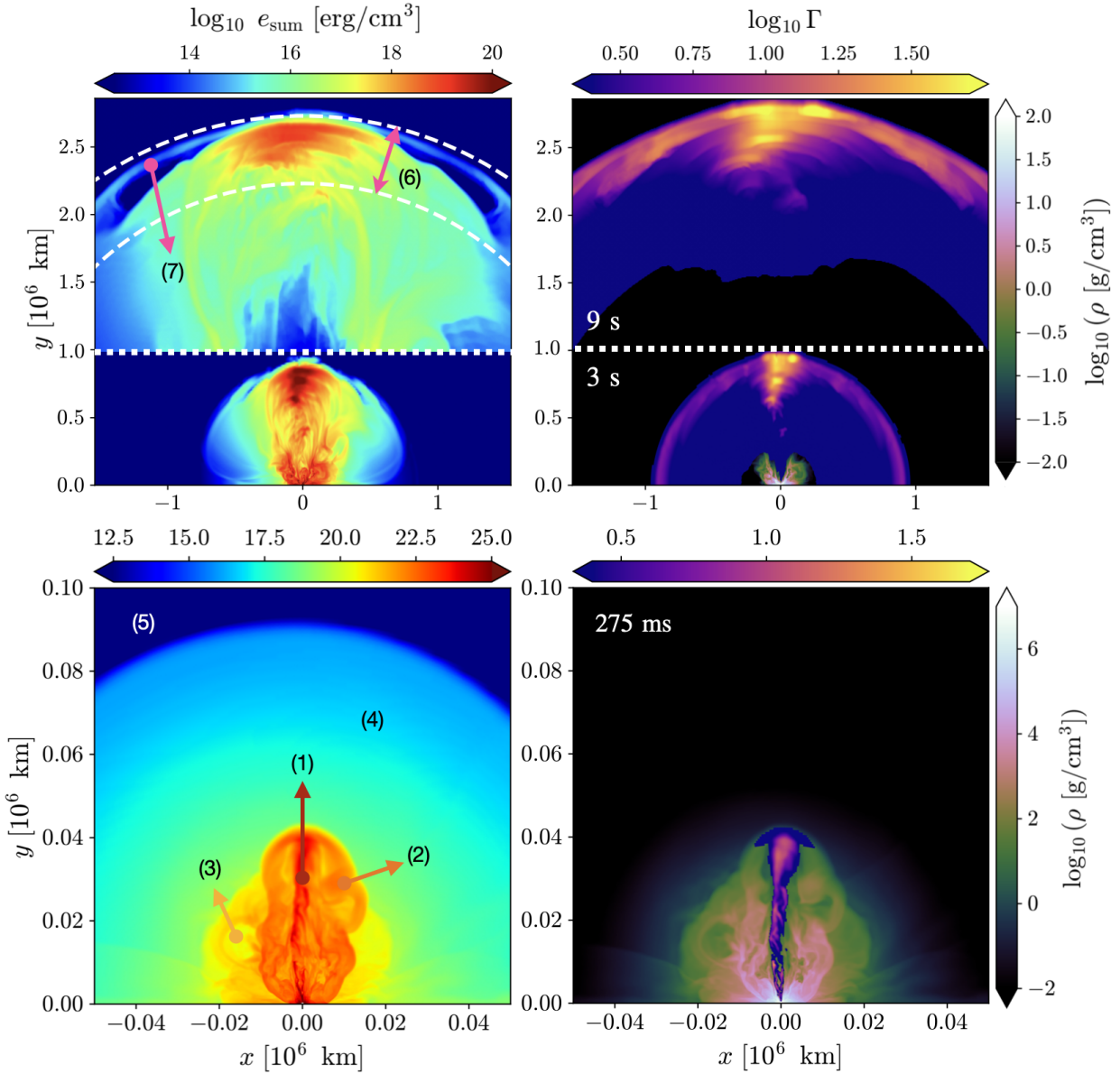


Fig. 1: Meridional view of total energy density excluding rest-mass contribution (e_{sum} ; left column) and rest-mass density and Lorentz factor (right column), at 275 ms (bottom), 3 s, and 9 s (top) after launch in the fiducial model F . The threshold in Γ is 1.5, 1.05 and 1.4 respectively for the three representative times. The top row shows composite panels combining snapshots at 3 and 9 s, referring to the former up to $y = 10^6$ km and to the latter above it. See text for the definition of the regions identified by numbers.

Model a , with its increased L_j , achieves the highest values of kinetic, thermal, and magnetic energy as soon as $\simeq 150$ ms after launch (we refer to the left panel of Figure 3 in P25). Model b initially evolves similarly to the fiducial case, but due to its longer τ_d , ultimately reaches an energy budget comparable to that of model a . By contrast, although models c and d feature increased magnetisation, model c evolves similarly to the fiducial case, whereas model d , with its lower L_j , produces an overall less energetic system. Finally, the low-luminosity and low-magnetisation models $e1$ and $e2$, which differ in launching time, yield very different outcomes: in the former, the strong jet-environment interaction leads to an overall lower-energy system, especially at the jet cap; in the latter, the much lower energy deposition into the environment results in a jet cap energetically comparable to those in models a and b . To quantify the energy budget of the different models, in Table 1 we list the maximum values of the

isotropic equivalent energy ($E_{\text{iso,max}}$; see Eq. 35 in P25), computed at the jet cap at t_{end} . We notice that models a and b yield comparable $E_{\text{iso,max}}$, a factor $\simeq 1.7 - 2$ larger than that of model $e2$, and more than twice those of models F , c , and d . Model $e1$ stands out, with a maximum energy being more than four times lower than those of models a and b .

During the evolution, thermal and magnetic energies are progressively converted into kinetic form, driving continued jet acceleration. This process eventually saturates as the jet enters the ballistic regime. Specifically, at $t - t_j = 3$ s, the fraction of energy at the jet cap in kinetic form ranges from 86% to 92% across the models (refer to Table 2 in P25). At $t - t_j = 6$ s, such a fraction reaches approximately 95% for model a , 93% for model b , 96% for model F , 94% for models c , d , $e1$, and 96% for model $e2$. Finally, by t_{end} , all models approach a saturation regime, with kinetic energy fractions between 95% and 97%. Notably, the

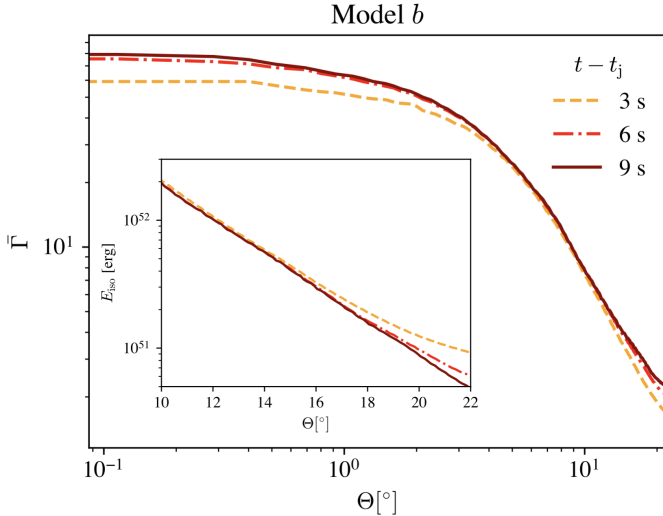


Fig. 2: Radially and azimuthally averaged Lorentz factor, and the corresponding E_{iso} at $\Theta > 10^\circ$ (inset), at the jet cap in model *b* at different evolutionary times. See text for discussion.

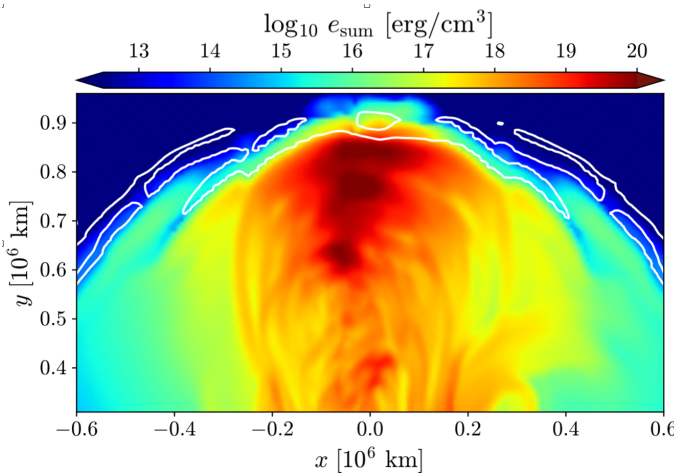


Fig. 3: Meridional view of the total (minus rest-mass) energy density at $t - t_j = 3$ s for model *F*. White contours identify shocked surfaces (see text).

relative increase in kinetic energy between 3 and 6 s is much larger than that between 6 and 9 s, reflecting the saturating trend in residual jet acceleration.

The evolution of the bulk Lorentz factor at the jet cap offers a complementary view of the above acceleration process and its saturating trend. Tracking the maximum of the radially and azimuthally averaged (axisymmetrised) Lorentz factor ($\bar{\Gamma}_{\text{max}}|_{\Phi_{\text{avg}}}$; see Eqs. 2 and 4 in D25), we find an average increase of about 4% across the models, with the exception of model *b*, which, owing to its longer τ_d , undergoes the most prolonged energy conversion period. As shown in Figure 2, the maximum relative change in $\bar{\Gamma}_{\text{max}}|_{\Phi_{\text{avg}}}$ between $t - t_j = 3$ and 6 s for model *b* is approximately 34%, decreasing to 14% between 6 and 9 s (t_{end}).

In the inset of Figure 2, we show the azimuthally averaged distribution of E_{iso} at $\Theta > 10^\circ$, in model *b*, which highlights the residual energy redistribution at large polar angles over time. Notably, the change in the slope of the distribution diminishes toward t_{end} , confirming that the jet is approaching a stable angular configuration.

We therefore consider t_{end} a late enough time to extract energy and velocity distributions for synthetic afterglow modelling.

2.7. Multiple shock structure

As described in Section 2.2, during its dynamical evolution the jet experiences a sharp transition as it emerges from the inner merger environment into a region of significantly lower external density, the outer merger environment, at the moment of breakout. The sudden change in density leads to the formation of a complex, multi-layered shock structure. At the forefront, a quasi-spherical outer shell propagates into the surrounding medium with an almost isotropic morphology, carrying a non-negligible energy budget compared to that of the cocoon itself. Notably, this leading shell is causally disconnected from the jet and its cocoon, which follow behind. Likely, its origin lies in the compression and acceleration of the fluid during the jet-cocoon breakout. Figure 3 shows again the snapshot at $t - t_j = 3$ s of e_{sum}^2 , where shocked regions are identified by the white contours as the boundaries where the fluid switches from subsonic to supersonic regime, i.e. the Mach number transitions from less to greater than one. The sound speed for the TM EOS is computed using Eq. (17) of Mignone & McKinney (2007).

The outer shell structure is of particular interest from an observational point of view, and is observed in all our jet simulations. At viewing angles $\theta_v \gtrsim 15^\circ$, where the observer does not have a direct line of sight into the jet core, this shell contributes to an excess of energy at relativistic velocities in the angular distribution of the ejecta. In synthetic afterglow light curves, this manifests as an early, shallow peak in the emission, preceding the steeper rise typically associated with the decelerating cocoon or the structured jet core (see the discussion in Section 4.1). This feature provides a distinct observational signature of the complex energy structure that the shock breakout imprints on the outflow.

3. Angular distribution of the jet material

Understanding the angular distribution of energy is crucial for interpreting afterglow light curves and for connecting theoretical models to observed GRB signatures, especially in cases of off-axis viewing angles. The morphology of the jet, its degree of symmetry, and the presence of fast-moving material at large angles all influence the observables.

Figure 4 displays the front-view distribution of the isotropic-equivalent energy, E_{iso} (see Eq. 3 of D25), evaluated in the jet cap at t_{end} . The red line shows the smallest contour that encloses 50% of the total energy, providing an estimate for the angular size of the jet's energetic core. A white cross marks the jet's barycentre, defined as the energy-weighted centroid in angular coordinates. The offset of this point from the centre (Θ_{off}) quantifies the jet's axis displacement relative to the injection axis and provides insight into the degree of asymmetry introduced by the interaction with the environment or internal jet instabilities.

Indeed, none of the simulated jets shows an axisymmetric distribution, and we find that the barycentre is displaced from the injection axis by $0.9^\circ - 3.6^\circ$ (see Table 1).

We define the effective half-opening angle Θ_{50} as the aperture angle of a cone subtending the same solid angle as that contained within the red contour. For all models, this is around 5° , with the smallest aperture given by model *e2* (4.6°), and

² For clarity, we report the plot only for a representative model (case *F*), as a similar structure develops for all models.

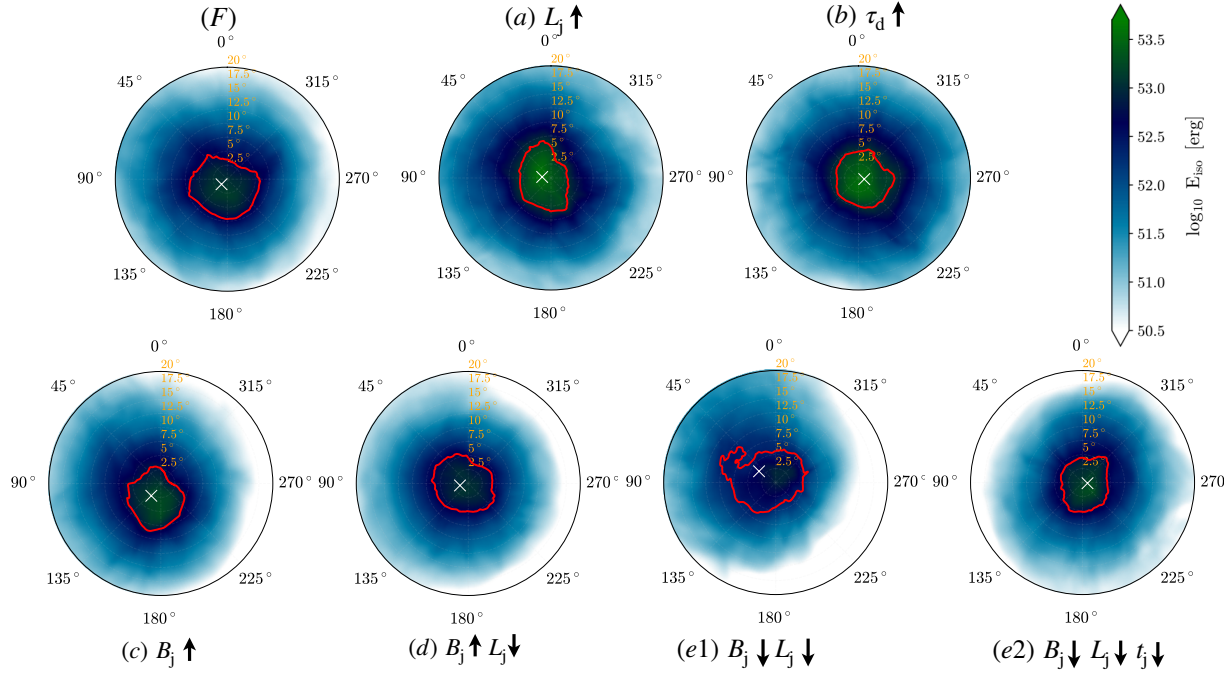


Fig. 4: Front-view distributions of the isotropic-equivalent energy of the jet cap for all jet models at t_{end} . The red line shows the smallest contour that contains 50% of the energy; the white cross indicates the jet's energy barycentre.

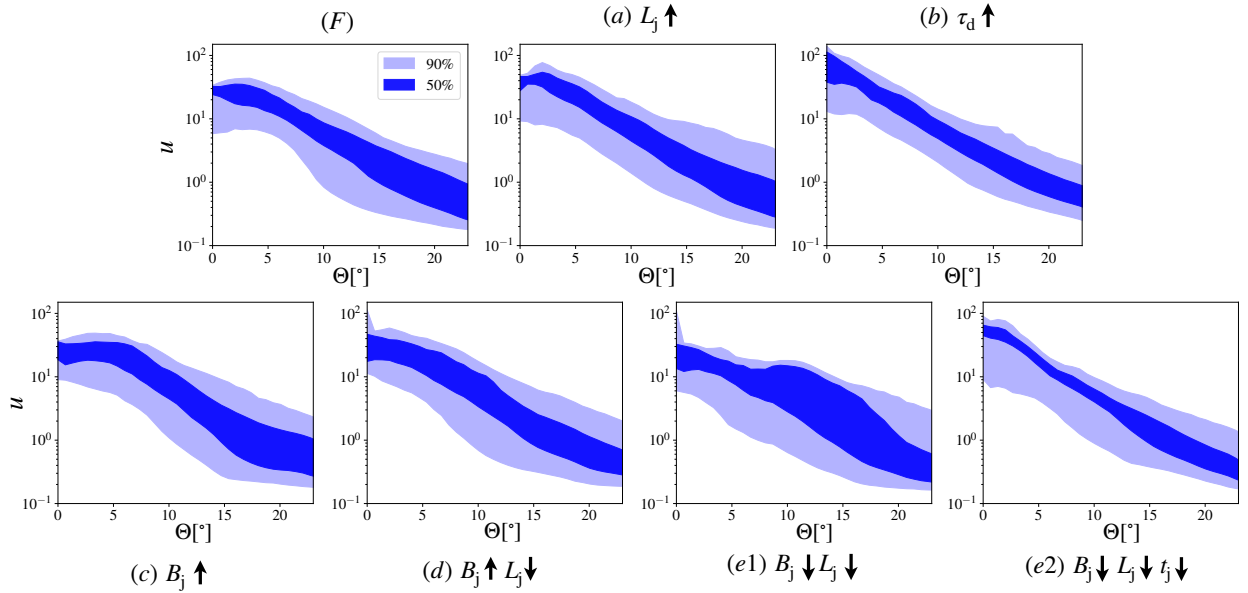


Fig. 5: Jet energy distribution in the four velocity-polar angle plane. The dark blue shaded region identifies the interquartile range (25th–75th percentiles) while the range between the 5th and 95th percentiles is shown in light blue.

the largest by model *e1* (6.1° , see Table 1). Models *a* and *b*, which have the highest injected energies, also feature the highest peak isotropic-equivalent energies. Model *b* is particularly well-collimated and shows a roughly circular, centrally peaked energy profile, consistent with standard expectations for successful, structured GRB jets.

The impact of magnetisation is explored through models *c* and *d*, which exhibit only minor deviations from the fiducial case (*F*) in terms of energy distribution and angular width.

The comparison between models *e1* and *e2* – which differ only in their jet launching time – highlights the importance of the central engine's timing relative to the collapse dynamics. Both models correspond to relatively weak jets, but their final angular structure differs significantly. Model *e2*, like model *b*, develops a narrow, energetic, and well-centred core, while model *e1* exhibits a less energetic, irregular core that is significantly misaligned. This underscores how earlier jet launching leads to re-

duced interaction with the ambient medium, preserving the jet's structure.

To further characterise the jet, we examine the joint distribution of energy in angular and velocity space. Figure 5 shows the energy distribution in the $\Theta-u$ plane, where $u \equiv \Gamma\beta$ is the modulus of the four-velocity of the fluid in units of the speed of light. For each polar angle Θ , we extract the percentiles of the energy distribution in u , calculated from the cumulative azimuthally averaged velocity profiles (see Appendix A). Specifically, we show the interquartile range (25th–75th percentiles, dark blue) and the broader range between the 5th and 95th percentiles (light blue). In the following, we refer to the n^{th} percentile for the four-velocity as u_n . This diagnostic reveals not just how fast the fluid is moving at each angle, but how widely the energy is distributed across different speeds.

At small angles ($\Theta \lesssim 4^\circ$), many profiles are relatively flat or display modest peaks around $\Theta \approx 2^\circ$, which are likely a by-product of the jet axis misalignment. In these regions, the typical u values are between 30 and 60, corresponding to ultra-relativistic bulk Lorentz factors. However, the substantial width of the distribution – even at small angles – reveals a broader velocity structure than commonly assumed. The presence of slower, though still relativistic material ($\Gamma \sim 3-10$) within the core implies that the outflow is not a uniform shell, but a stratified structure composed of multiple shells with a relatively wide range of Lorentz factors.

Beyond $\Theta \approx 4^\circ$, the median and upper percentile curves decline gradually, with u_{95} remaining above 10 up to $\Theta \approx 15^\circ$. This indicates that a small amount of fast-moving material persists even at relatively large angles from the jet axis. The presence of this high-velocity material in the jet's wings is likely related to the complex jet structure presented in Section 2.7.

At larger angles ($\Theta \gtrsim 20^\circ$), the outflow becomes dominated by sub-relativistic material ($u \lesssim 1$), and the velocity distribution becomes increasingly skewed towards low u . Nevertheless, small amounts of faster material are still present at these wide angles, though their energy content is comparatively small.

The above results suggest that these jets have a high degree of angular and velocity stratification, with a fast, collimated core surrounded by slower, less energetic wings. The transition between these regions is smooth rather than abrupt, challenging simplistic ‘top-hat’ and ‘two component’ jet models and highlighting the possibility of long-lasting energy injection in the external shock at all angles due to the broad velocity profiles, pointing to the need for more nuanced, structured outflows in afterglow modelling.

To facilitate the comparison with analytical jet structures, in Figure 6 we show the azimuthally averaged $E_{\text{iso}}^{\Phi_{\text{avg}}}(\Theta)$ profiles at t_{end} for all the models. All jet simulations feature a flat energetic core for $\Theta \leq 2-3^\circ$. The less energetic wings are characterised by multiple segments with different slopes, affecting the rising part of the afterglow light curves for off-axis observers (see Section 4.1). For angles $\Theta > 10^\circ$, we compare the profiles to a power-law structure $\propto \Theta^{-a}$. All models roughly follow $a \approx 6$, with the exception of model *e1* showing a shallower decay $\propto \Theta^{-4}$. A Gaussian profile is also shown in comparison to model *a*. We conclude that our results do not generally support a structure described by a power-law or a Gaussian profile.

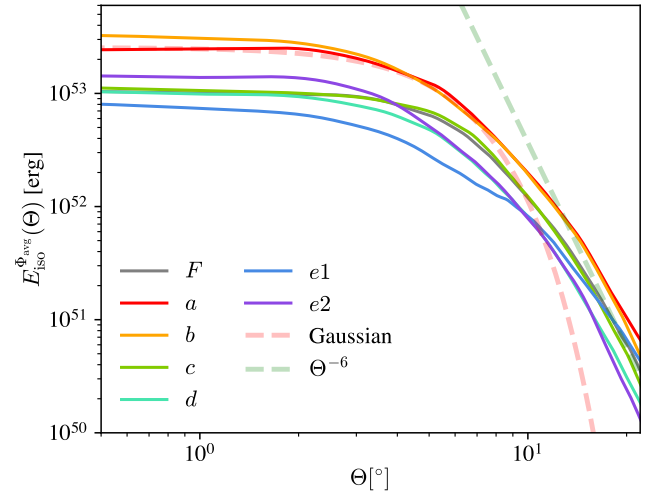


Fig. 6: $E_{\text{iso}}^{\Phi_{\text{avg}}}(\Theta)$ profiles for all jet models at t_{end} .

4. Afterglow light curves

4.1. The model

To compute the broadband afterglow emission from our simulated jets, we employ a semi-analytical model based on Salafia et al. (2019, 2022), tailored for relativistic outflows with both angular and velocity structure. The model computes synchrotron emission from shock-accelerated electrons in a decelerating relativistic blast wave. The version of the model used in this work introduces two critical updates to better reflect the physical complexity revealed by our 3D simulations. First, the code has been extended to incorporate the radial velocity profile of the jet extracted from the simulation data, as described in Appendix B. Instead of treating the outflow as a uniform shell with a single Lorentz factor at each angle, we consider the distribution of energy across fluid elements with different four-velocities, u . This allows us to model energy injection from slower shells catching up with the shock front, a process that is especially important during the rising phase of the afterglow light curve. Second, the assumption of axisymmetry is relaxed. Light curves are computed directly from the full 3D energy and velocity distributions, including azimuthal variations. This is essential for capturing the observational signatures of asymmetric outflows, which can differ substantially from their azimuthally averaged counterparts, particularly for off-axis observers.

Together, these upgrades allow us to more accurately predict the emission from realistic GRB jets and to explore the consequences of internal structure and asymmetry on the observed light curves. We caution, though, that the model does not include the effects of lateral expansion of the shock, which are likely relevant at late enough times.

4.2. Choice of reference parameters

In order to compute the afterglow light curves from the blast-waves caused by our simulated outflows, we need to specify a number of additional parameters: the number density n of the external medium (assumed homogeneous); the ‘micro-physical’ parameters that describe the fraction of the shock downstream internal energy in relativistic electrons (ϵ_e), the fraction in turbulent magnetic field (ϵ_B) and the slope of the power law energy

Table 2: Result of MCMC fitting of each model to GW170817 afterglow data.

Parameter	Prior ^(a)	Fit results ^(b)						
		<i>F</i>	<i>a</i>	<i>b</i>	<i>c</i>	<i>d</i>	<i>e1</i>	<i>e2</i>
$\log(n/\text{cm}^{-3})$	$\mathcal{U}(-5, -1)$	-1.5 ± 0.3	$-1.2^{+0.2}_{-0.25}$	$-1.2^{+0.2}_{-0.3}$	-1.5 ± 0.3	-1.6 ± 0.3	$-1.04^{+0.04}_{-0.06}$	-2.0 ± 0.4
$\log(\epsilon_B)$	$\mathcal{U}(-8, -1)$	-6.25 ± 0.11	-7.29 ± 0.07	-7.50 ± 0.08	-6.4 ± 0.1	-6.1 ± 0.1	-5.58 ± 0.03	-6.45 ± 0.13
θ_v/deg	Isotropic	24.3 ± 2.1	22.5 ± 1.2	21.2 ± 1.2	$24.3^{+1.9}_{-1.8}$	23.5 ± 2.0	31.75 ± 0.55	18.6 ± 2.0

^(a) ‘ $\mathcal{U}(a, b)$ ’ means uniform between a and b ; ‘Isotropic’ means uniform in the cosine of the angle. ^(b) Median and 90% credible interval of the marginalised posterior probability of each of the models.

distribution of the accelerated relativistic electrons (p); the redshift z and luminosity distance d_L of the source; the polar and azimuthal viewing angles, θ_v and ϕ_v .

In order to compare the light curves with observations we focus on the afterglow associated to GW170817. Thus, we set the redshift to $z = 0.0096$ and luminosity distance to $d_L = 40 \text{ Mpc}$ (Cantiello et al. 2018). Moreover, we fix $\epsilon_e = 0.1$, based on theoretical expectations (Sironi et al. 2013), and we set $p = 2.166$, as constrained by multi-wavelength observations of the GW170817 synchrotron emission (Fong et al. 2019). This leaves us with four free parameters, namely $(n, \epsilon_B, \theta_v, \phi_v)$.

We obtained reference values of n , ϵ_B and θ_v for each of our models by fitting the GW170817 data from Makhathini et al. (2021) adopting the axisymmetrised version of our jet structures at t_{end} . The fit was performed through a Markov Chain Monte Carlo (MCMC) technique as implemented in the `emcee` python package (Foreman-Mackey et al. 2013). We assumed a log-uniform prior on n in the range $(10^{-5}, 10^{-1}) \text{ cm}^{-3}$, where the lower limit is informed by the smallest densities expected in galactic outskirts (Fong et al. 2015), while the upper limit is informed by observations of the GW170817 environment (Hajela et al. 2019); we set the prior on ϵ_B as log-uniform in the range $(10^{-8}, 10^{-1})$, where the lower end is set by a loose requirement that the magnetic field in the shock downstream does not fall below typical intergalactic values, while the upper value is informed by theoretical expectations from particle-in-cell simulations of relativistic shocks (Sironi et al. 2013); we set the prior on θ_v as isotropic, that is, uniform in $\cos \theta_v$ between -1 and 1.

The results of the fitting procedures are reported in Table 2, and the 3 GHz best-fit light curve³ of model *F* is shown in Figure 11 (see Appendix C for the other models). Corner plots of the posterior probability distributions are also shown in Appendix C (Figs. C.3 and C.4). The results show a general preference for very low values of $\epsilon_B \lesssim \text{few} \times 10^{-6}$ combined with high values of $n \gtrsim 0.01 \text{ cm}^{-3}$, in some tension with observational indications of a low density environment (Hajela et al. 2019). The best fit viewing angles θ_v fall in the limited range between 19 and 24 degrees, with the exception of model *e1* (giving about 32 degrees). We note that only the lower end of the above interval is in agreement with the constraints imposed by the observation of apparent superluminal motion of the afterglow centroid with radio very long baseline interferometry (Mooley et al. 2018b; Ghirlanda et al. 2019; Nakar & Piran 2021; Mooley et al. 2022; Govreen-Segal & Nakar 2023; Gianfagna et al. 2024). A more detailed study that includes the modelling of the radio centroid

displacement may therefore show that some of our simulated outflows are not compatible with observations of GW170817.

4.3. Impact of velocity profile

In Figure 7 we compare afterglow light curves for the fiducial model *F* computed with and without the inclusion of the velocity profile, adopting the values of n , ϵ_B and θ_v best-fitting GW170817 afterglow data (see Table 2). In addition, we consider the on-axis case ($\theta_v = 0$). Here and in the following, we show in particular the light curves obtained at 3 GHz. We recall that, in the case without the velocity profile, all material at a given angle is assigned a single Lorentz factor, corresponding to an ‘average’ saturation value computed from the total energy of the outflow. At this stage, we still refer to the azimuthally averaged jet profiles. The assumption of axisymmetry will be relaxed in Section (4.5).

The most immediate effect of including the velocity profile is a broadening of the light curve, especially in its early rising phase. The sharp rise seen in the simplified case becomes more gradual, as slower inner shells catch up with the forward shock, injecting energy over time. This is a natural consequence of the stratified structure seen in the simulations, where the energy is distributed over a relatively wide range of four-velocities even near the jet axis (see Fig. 5).

Additionally, the quasi-spherical outer shell accompanying the expanding jet (Section 2.7) gives rise to a secondary, dimmer peak at early times, visible at off-axis viewing angles.

Due to its intrinsically low luminosity and early occurrence, this feature is likely below the detection threshold of current X-ray and radio observatories.⁴ Nevertheless, it represents a potential diagnostic for structured jets to be considered in the future, as higher sensitivity observations and early afterglow follow-up become accessible.

4.4. Light curves at different evolution times

To assess the importance of extending the jet simulations beyond the initial evolutionary phase, we compare afterglow light curves computed from outflow data at different post-launch times. Specifically, we contrast results obtained at $t - t_j = 3 \text{ s}$, the endpoint of the jet simulation presented in P25, with those at the end of our extended 3D simulation (i.e. at $t_{\text{end}} = 9 \text{ s}$). The goal of this comparison is to understand how the continued evolution of the outflow affects observable quantities. During the early post-breakout phase, the jet undergoes significant reorganisation: residual acceleration, cocoon expansion, and mixing can all reshape the angular and velocity structure of the outflow.

⁴ The non-axisymmetrized jet structure of model *b* seems however more promising in this sense, as shown in Fig. C.2

³ The best-fit models are obtained using the full set of available multi-band observations of GW170817. We find that our conclusions are consistent across comparisons with data in the optical, X-ray, and radio bands. Since the radio band provides the most extensive data coverage, for simplicity all light curves presented in this work are computed at a frequency of 3 GHz.

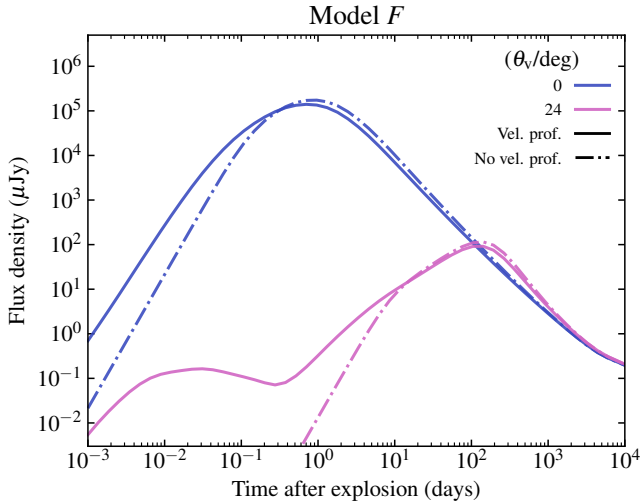


Fig. 7: Afterglow light curve at 3 GHz for the fiducial case at t_{end} , with or without the inclusion of the velocity profile in the afterglow model, for both an on-axis and an off-axis observer.

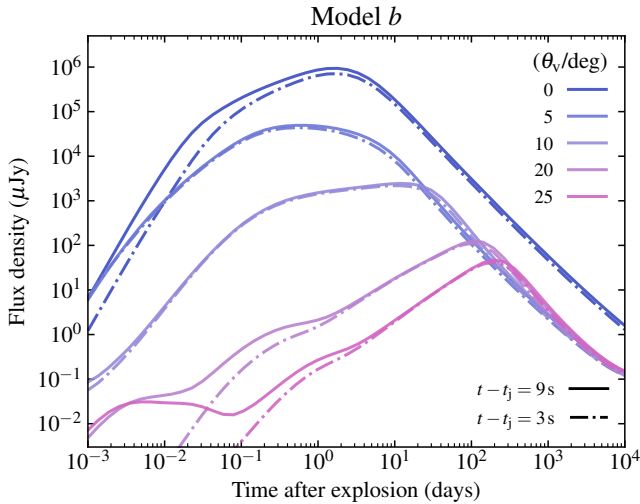


Fig. 8: Afterglow light curve at 3 GHz for model *b* at the beginning and at the end of the extended evolution, considering a set of viewing angles θ_v

These effects are not captured in models that truncate shortly after breakout.

In Figure 8, we show such a comparison for model *b*, considering the azimuthally averaged jet profiles and different viewing angles θ_v . Our results show that the later-time simulations predict noticeable differences in the early rising phase of the light curve. In fact, while the late-time behaviour (decay slope) is identical across the two snapshots, the early light curve is sensitive to the detailed structure at different evolutionary times.

This confirms the value of extending jet simulations to at least ~ 10 s, especially for interpreting the rising phase of the afterglow, which is crucial for constraining jet geometry, energy, and viewing angle.

4.5. Impact of azimuthal asymmetries

Here, we investigate the impact of azimuthal asymmetries in the jet structure on the resulting afterglow light curves. The extent and origin of such deviations from axisymmetry is discussed in Section 3.

In Figure 9, we show light curves for the fiducial model and an on-axis observer ($\theta_v = 0$), comparing results obtained from the axisymmetrised ('AS') and non-axisymmetrised ('NAS') jet structure. We observe negligible difference between the two curves.

In Figure 10, we compare the axisymmetrised and non-axisymmetrised cases for a slightly off-axis observer ($\theta_v = 3^\circ$) and at four different azimuthal viewing angles $\phi_v = (0, 1, 2, 3) \times \pi/2$. This allows us to highlight the effects of structural asymmetries. We find that varying the azimuthal viewing angle can produce order-of-magnitude differences in the rising part and the peak of the light curve, which then decrease after the peak and become negligible (this is even more evident for model *a*, as shown in C.2).

In Fig. 11 we perform a similar analysis but for a strongly off-axis observer ($\theta_v = 24^\circ$, i.e. the best-fitting value with respect to GW170817 data; see Table 2). Also in this case, varying the azimuthal angle produces large differences up to the peak time. We find that the early-time peak due to the multiple-shock structure, for off-axis observers, is strongly dependent on the azimuthal viewing angle. This indicates that the energetic shells responsible for the early-time emission are not uniformly distributed along the azimuthal direction.

Finally, we performed MCMC best-fit analysis for model *F* (see Section 4.2) by employing the non-axisymmetrised jet structure, for three different azimuthal viewing angles, i.e. $\phi_v = 0, \pi/2, \pi$ (corner plots are shown in Appendix C, Fig. C.5). We find substantial differences in the parameter estimations with the different azimuthal viewing angles and with respect to the axisymmetrised case. Focusing on the estimation of the polar viewing angle, we find $\theta_v \simeq 32^\circ \pm 1^\circ, 22^\circ \pm 3^\circ, 25^\circ \pm 3^\circ$ degrees for the three choices of ϕ_v , respectively. In particular, we note that for $\phi_v = 0$, the estimation of θ_v is not compatible with the one obtained from the axisymmetrised structure (within 90% credi-

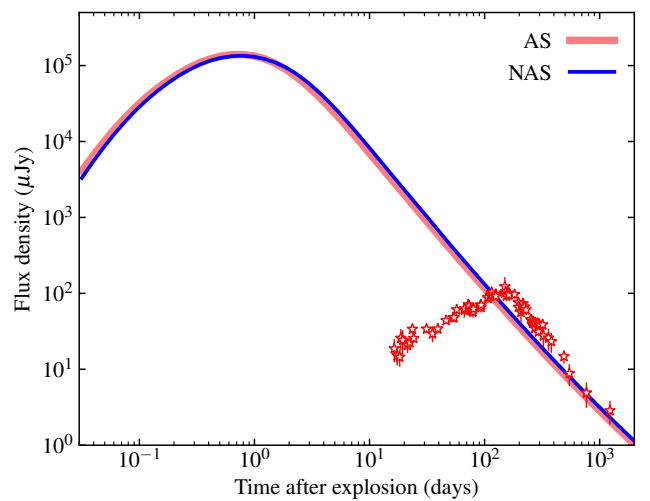


Fig. 9: On-axis afterglow light curves at 3 GHz computed using the axisymmetrised (AS – thick red line) and not axisymmetrised (NAS – blue line) jet profiles from model *F*. Red stars with vertical error bars correspond to the GW170817 afterglow data.

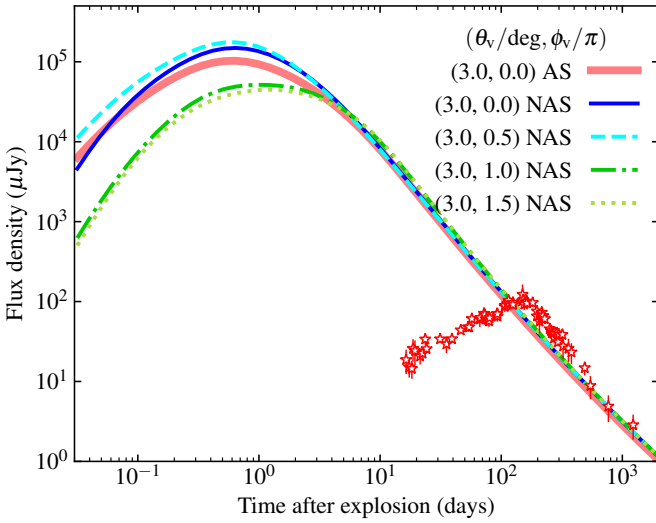


Fig. 10: Analogous to Fig. 9 for slightly off-axis observation angle ($\theta_v = 3^\circ$). In the non-axisymmetrised (NAS) case, we also vary the azimuthal viewing angle ϕ_v .

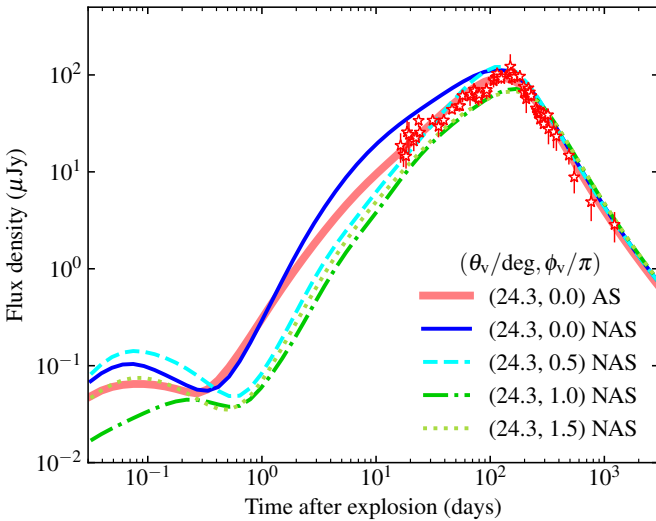


Fig. 11: Analogous to Fig. 10 for $\theta_v = 24^\circ$.

ble intervals). Similar considerations also apply to the estimates of the other two free parameters, n and ϵ_B .

In summary, asymmetries in the jet structure lead to anisotropic emission patterns, especially at early times and for off-axis observers. This implies an intrinsic, commonly overlooked uncertainty in evaluating the afterglow parameters (including the viewing angle θ_v) when interpreting the observations under the assumption of axisymmetry.

The full set of light curves for all jet models is presented in Appendix C.

4.6. Impact of jet injection parameters on afterglow light curves

In this Section, we assess how variations in the jet injection parameters shape the resulting afterglow light curves. Figure 12 compares the light curves obtained from the axisymmetrised versions of jet structures from the different models, computed with

a fixed set of afterglow parameters equal to the best-fit values of the fiducial case. We show the results for both on- and off-axis observers.

The rising phase of the off-axis light curves (shown in the top panel of the Figure) is primarily controlled by the jet's angular structure (Figure 6) and the presence of a velocity profile (Section 4.3). Steeper energy distributions outside the jet core lead to a correspondingly steeper rise, as progressively more energy enters the observer's line of sight when the jet decelerates and the relativistic beaming cone widens. Signatures of changes in slope in the energy distribution and the presence of different components in the velocity profile are directly imprinted on the light curves as breaks or slope changes during the rise.

The time scale t_{peak} of peak emission scales with the jet energy through the Sedov length R_S (i.e. the fundamental length scale of the problem, e.g. Blandford & McKee 1976), that is $t_{\text{peak}} \propto R_S/c \propto [E_{\text{iso}}(\Theta = 0)/n]^{1/3}$. More energetic and collimated jets (models *a*, *b*, and *e2*) peak indeed at later times. As seen from both the on- and off-axis curves (bottom and top panel of Figure 12, respectively), their peaks are also brighter, since a larger R_S corresponds to a greater number of emitting electrons.

Models *c* and *d* differ very little from the fiducial case, as expected due to the minor difference in luminosity and/or magnetisation. Comparing models *e1* and *e2*, which differ in jet launching time, we observe that *e2* produces a more typical afterglow evolution with a brighter and delayed peak, while *e1* presents an extended plateau prior to peak time, produced by its peculiar energetic structure. Model *e1* has indeed a less energetic, less collimated, and more off-centered jet core.

At late times, the decaying phase of the light curve is no longer sensitive to the jet structure, and the models converge to similar slopes.

5. Summary and outlook

In this work, we presented a set of 3D relativistic MHD simulations of jets emerging from a realistic binary neutron star merger environment, extending the work presented in (P25) to reach saturation in terms of jet structure and acceleration. Then, we used the output of our simulations to compute the afterglow emission of the different jets with an improved semi-analytic code, assessing the impact of the differences arising in the jets' structure with time and angle. Finally, we performed MCMC fits to the data of the GW1708017 event, obtaining the best-fit values for a subset of the afterglow model parameters.

From the dynamical evolution of the various jet models, given the specific choice for the input parameters we find that more energetic jets experience a more successful drilling through the merger environment, losing less energy with respect to the fiducial case. As a consequence, especially for a longer decay time scale for injection, the resulting jet structure is only slightly displaced from the injection axis and exhibits a more energetic core. The launching time has also major impact on the jet evolution, with jets launched earlier resulting in a more axisymmetric, collimated, and energetic core. Finally, increasing the magnetisation helps maintaining a more stable jet-environment interface, preventing the development of instabilities. Nevertheless, given the choice made for the input parameters, we do not find major differences in the evolution and final structure of the jet models with different magnetisation.

Despite the differences between the various models in the pre-breakout phase, which primarily influence the resulting jet energetics and structure, they all behave similarly in the late time evolution. Notably, we find that at the time of the jet-cocoon

breakout, all models develop a complex multiple-shock structure, with an outer shell of non negligible energy preceding the jet ejecta. This region is responsible for producing an early time dimmer peak in the afterglow light curves.

The effect of the specific radial and angular structure of the different jets (including also the outer shell mentioned above) is properly taken into account only if the jet's velocity profile is included in the afterglow dynamics.

The relevance of extending the simulations up to nine seconds, when acceleration is mostly over and the angular structure is no longer changing, is mostly evident in the early-time part of the light curves, especially for large viewing angles.

As previously shown in D25, we find that the 3D evolution within a realistic post-merger environment leads to asymmetries (i.e. deviations from axisymmetry) in the jet structure, especially for the weaker jets that are more affected by this interaction. The impact on the afterglow emission is investigated by relaxing the assumption of axisymmetry in the afterglow model, and comparing the resulting emission by varying both θ_v and ϕ_v .

While the on-axis emission remains nearly identical, for off-axis observers (θ_v above a few degrees) we find up to an order-of-magnitude differences in the flux density for different choices of ϕ_v .

Restricting to the axisymmetrised jet structures, the MCMC fits to the data of GW170817 for all our models allow us to obtain reference values for computing the afterglow light curves. We find that, in general, all the jet structures considered are compatible with the observational data of this event. The best-fit values favour polar viewing angles between 19 and 24 degrees (except for the model with the lowest injected energy and magnetisation, giving about 32 degrees), very low ϵ_B and rather high n .

To assess the impact of the different jet injection parameters in shaping the emission, we compare the light curves from the different configurations for a fixed set of afterglow parameters, corresponding to the best-fit values obtained for the axisymmetrised jet structure of the fiducial model. This comparison is made for both on-axis and off-axis observers. As expected, more energetic jets produce a brighter emission, peaking at later times. In particular, we find a difference of 1.5 orders of magnitude in the on-axis peak emission between the least and the most energetic jet models.

We conclude that even relatively small variations in the initial conditions of jet launching can have a non-negligible impact on the resulting afterglow light curves. This suggests that, in cases where the available observational information is sufficient to break degeneracies among afterglow parameters, tighter constraints on the jet initial conditions may be achievable. Structural asymmetries further increase the complexity of the problem by introducing additional effects in shaping the light curves. In this context, early-time observations, when available, are expected to play a key role in reducing parameter degeneracies.

We note that, while our results are robust across comparisons with optical, X-ray, and radio observations of GW170817, we focus on the radio band, at 3 GHz, due to its superior data coverage. Nevertheless, multi-band comparisons remain essential, particularly for future events where improved observational coverage across different wavelengths may provide stronger constraints.

Our analysis can benefit from different improvements in the future, such as the inclusion of the side expansion within the afterglow model or the computation of the radio centroid motion for a more informed comparison with the data. A possible extension of the angular analysis would be to study the effect of the structural asymmetries in terms of polarisation (see, e.g., Lamb

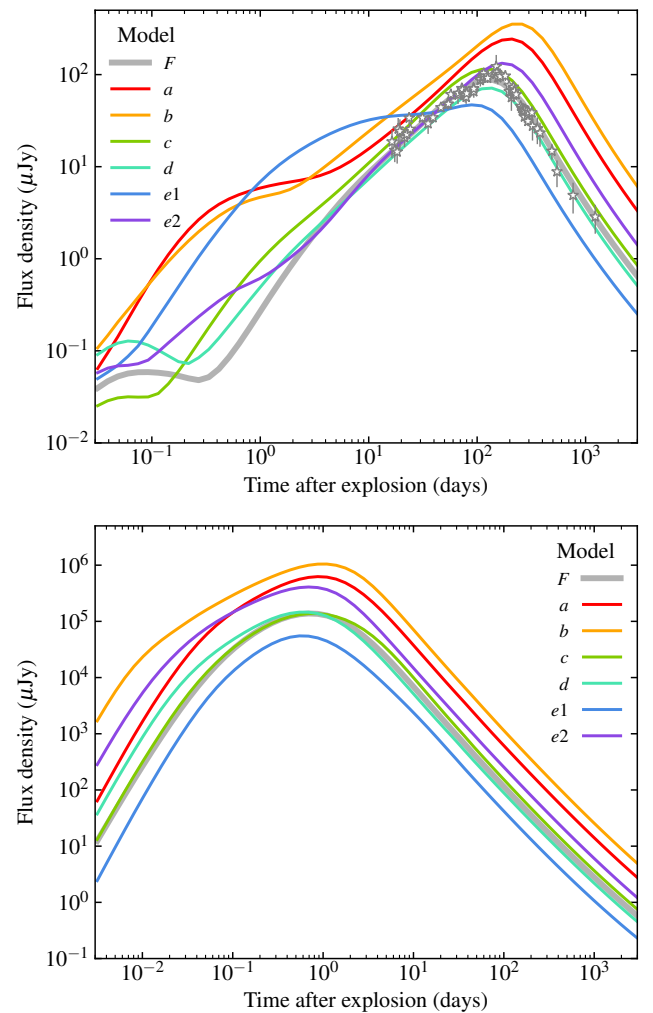


Fig. 12: Top: Comparison of afterglow light curves at 3 GHz obtained from the axisymmetrized jet structures of the different models, adopting a fixed set of afterglow parameters (namely, the best-fit values obtained for the fiducial model F , see Table 2). Grey stars with vertical error bars correspond to GW170817 data. Bottom: Analogous comparison for the on-axis observer ($\theta_v = 0$).

et al. 2022). Moreover, considering the non-axisymmetrised jet structures, the azimuthal viewing angle can be taken into account as an additional parameter of investigation. Finally, another possible future development would be to extend the parameter study to a broader range of input values, allowing a more systematic exploration of jet injection regimes relevant for GW170817-like events.

Acknowledgements. This work was supported by the European Union under NextGenerationEU, via the PRIN 2022 Projects “EMERGE: Neutron star mergers and the origin of short gamma-ray bursts”, Prot. n. 2022KX2Z3B (CUP C53D23001150006), and “PEACE: Powerful Emission and Acceleration in the most powerful Cosmic Explosion”, Prot. n. 202298J7KT (CUP G53D23000880006). The views and opinions expressed are solely those of the authors and do not necessarily reflect those of the European Union, nor can the European Union be held responsible for them. We further acknowledge support from the INAF Theory Grant 2023 “AfterJet: Modelling short gamma-ray burst jets from binary neutron star mergers and their afterglow emission”, Ob.Fu. 1.05.23.06.02 (CUP C93C23006800005). AP and RC acknowledge additional support by the Italian Ministry of Foreign Affairs and International Cooperation (MAECI), grant number US23GR08. OS acknowledges financial support from INAF through grant 1.05.23.04.04. Simulations were performed on the Discov-

erer HPC cluster at Sofia Tech Park (Bulgaria). We acknowledge EuroHPC Joint Undertaking for awarding us access to this cluster via the Regular Access allocation EHPC-REG-2023R03-160.

References

Abbott, B. P., Abbott, R., Abbott, T. D., et al. 2017a, *ApJ*, 848, L13
 Abbott, B. P., Abbott, R., Abbott, T. D., et al. 2017b, *Phys. Rev. Lett.*, 119, 161101
 Abbott, B. P., Abbott, R., Abbott, T. D., et al. 2017c, *ApJ*, 848, L12
 Berger, E. 2014, *ARA&A*, 52, 43
 Blandford, R. D. & McKee, C. F. 1976, *Physics of Fluids*, 19, 1130
 Cantiello, M., Jensen, J. B., Blakeslee, J. P., et al. 2018, *ApJ*, 854, L31
 Ciolfi, R. 2020, *MNRAS*, 495, L66
 Dreas, E., Pavan, A., Ciolfi, R., & Celotti, A. 2025, *A&A*, 694, A200
 Eichler, D., Livio, M., Piran, T., & Schramm, D. N. 1989, *Nature*, 340, 126
 Fong, W., Berger, E., Margutti, R., & Zauderer, B. A. 2015, *ApJ*, 815, 102
 Fong, W., Blanchard, P. K., Alexander, K. D., et al. 2019, *ApJ*, 883, L1
 Foreman-Mackey, D., Hogg, D. W., Lang, D., & Goodman, J. 2013, *PASP*, 125, 306
 Fraija, N., Kamenetskaia, B. B., Galvan-Gamez, A., et al. 2022, *ApJ*, 933, 243
 Ghirlanda, G., Salafia, O. S., Paragi, Z., et al. 2019, *Science*, 363, 968
 Gianfagna, G., Piro, L., Pannarale, F., et al. 2024, *MNRAS*, 528, 2600
 Gill, R., Nathanail, A., & Rezzolla, L. 2019, *ApJ*, 876, 139
 Gottlieb, O., Issa, D., Jacquemin-Ide, J., et al. 2023, *ApJ*, 954
 Gottlieb, O., Moseley, S., Ramirez-Aguilar, T., et al. 2022, *ApJ*, 933, L2
 Gottlieb, O., Nakar, E., & Piran, T. 2017, *MNRAS*, 473, 576
 Govreen-Segal, T. & Nakar, E. 2023, *MNRAS*, 524, 403
 Granot, J. & van der Horst, A. J. 2014, *PASA*, 31, e008
 Hajela, A., Margutti, R., Alexander, K. D., et al. 2019, *ApJ*, 886, L17
 Kathirgamaraju, A., Tchekhovskoy, A., Giannios, D., & Barniol Duran, R. 2019, *MNRAS*, 484, L98
 Komissarov, S. S., Vlahakis, N., Königl, A., & Barkov, M. V. 2009, *MNRAS*, 394, 1182
 Lamb, G. P., Levan, A. J., & Tanvir, N. R. 2020, *ApJ*, 899, 105
 Lamb, G. P., Nativi, L., Rosswog, S., et al. 2022, *Universe*, 8, 612
 Lazzati, D., Perna, R., Morsony, B. J., et al. 2018, *Phys. Rev. Lett.*, 120, 241103
 Lyutikov, M. 2020, *MNRAS*, 491, 483
 Makhathini, S., Mooley, K. P., Brightman, M., et al. 2021, *ApJ*, 922, 154
 Mészáros, P. & Rees, M. J. 1997, *ApJ*, 476, 232
 Mignone, A., Bodo, G., Massaglia, S., et al. 2007, *ApJS*, 170, 228
 Mignone, A. & McKinney, J. C. 2007, *MNRAS*, 378, 1118
 Mignone, A., Plewa, T., & Bodo, G. 2005, *ApJS*, 160, 199
 Mignone, A. & Tzeferacos, P. 2010, *Journal of Computational Physics*, 229, 2117
 Mignone, A., Tzeferacos, P., & Bodo, G. 2010, *Journal of Computational Physics*, 229, 5896
 Mooley, K. P., Anderson, J., & Lu, W. 2022, *Nature*, 610, 273
 Mooley, K. P., Deller, A. T., Gottlieb, O., et al. 2018a, *Nature*, 561, 355
 Mooley, K. P., Nakar, E., Hotokezaka, K., et al. 2018b, *Nature*, 554, 207
 Moss, M. J., Mochkovitch, R., Daigne, F., Beniamini, P., & Guiriec, S. 2023, *MNRAS*, 525, 5224
 Murguia-Berthier, A., Montes, G., Ramirez-Ruiz, E., De Colle, F., & Lee, W. H. 2014, *ApJ*, 788, L8
 Nakar, E. 2020, *Phys. Rep.*, 886, 1
 Nakar, E. & Piran, T. 2021, *ApJ*, 909, 114
 Narayan, R., Paczynski, B., & Piran, T. 1992, *ApJ*, 395, L83
 Nativi, L., Bulla, M., Rosswog, S., et al. 2021, *MNRAS*, 500, 1772
 Nativi, L., Lamb, G. P., Rosswog, S., Lundman, C., & Kowal, G. 2022, *MNRAS*, 509, 903
 Nava, L., Sironi, L., Ghisellini, G., Celotti, A., & Ghirlanda, G. 2013, *MNRAS*, 433, 2107
 Pais, M., Piran, T., Kiuchi, K., & Shibata, M. 2024, *ApJ*, 976, 35
 Panaitescu, A. & Kumar, P. 2000, *ApJ*, 543, 66
 Panaitescu, A., Mészáros, P., & Rees, M. J. 1998, *ApJ*, 503, 314
 Pavan, A., Ciolfi, R., Dreas, E., & Kalinani, J. V. 2025, *MNRAS*, 540, 1345
 Pavan, A., Ciolfi, R., Kalinani, J. V., & Mignone, A. 2021, *MNRAS*, 506, 3483
 Pavan, A., Ciolfi, R., Kalinani, J. V., & Mignone, A. 2023, *MNRAS*, 524, 260
 Pe'er, A. 2012, *ApJ*, 752, L8
 Salafia, O. S., Ghirlanda, G., Ascenzi, S., & Ghisellini, G. 2019, *A&A*, 628, A18
 Salafia, O. S., Ravasio, M. E., Yang, J., et al. 2022, *ApJ*, 931, L19
 Sari, R. & Mészáros, P. 2000, *ApJ*, 535, L33
 Sari, R., Piran, T., & Narayan, R. 1998, *ApJ*, 497, L17
 Sironi, L., Spitkovsky, A., & Arons, J. 2013, *ApJ*, 771, 54
 Tchekhovskoy, A., Narayan, R., & McKinney, J. C. 2010, *New A*, 15, 749
 Woosley, S. E. 1993, *ApJ*, 405, 273
 Zhang, B., Fan, Y. Z., Dyks, J., et al. 2006, *ApJ*, 642, 354

Appendix A: Velocity profile

The velocity profiles extracted from our simulations provide crucial input for modelling the jet's afterglow. Specifically, they allow us to track how much energy is carried by fluid elements at each angle and four-velocity. In the simplest jetted GRB models, all of the energy is uniformly distributed within a narrow angular region around the axis and is carried by ultra-relativistic material with a single, definite Lorentz factor. A more complex distribution of energy in the angle and in the Lorentz factor space leads to a more rich phenomenology, especially when the viewing angle is allowed to vary.

Figure C.1, represents velocity profiles at different Θ angles (identified by different colours) for the fiducial model at t_{end} , obtained from the azimuthally averaged (total) energy distribution. As already pointed out in Section 3, we note that even at small angles from the injection axis the profiles are wide, indicating that a considerable amount of energy is carried by slower elements.

Moreover, we find that some high-velocity material exists even at large angles ($\Theta > 15^\circ$), albeit in small quantities. This component originates from the jet's multiple-shell structure (see Section 2.7) and can produce observable signatures, particularly for off-axis observers (see Section 7).

Appendix B: Blastwave dynamics

We compute the dynamics of the blastwave independently at each angular coordinate (Θ, Φ) (therefore neglecting lateral energy transport) based on an approximate conservation of energy per unit solid angle. Let us assume that the isotropic-equivalent energy of the outflow E_{iso} is entirely in the form of kinetic energy plus rest mass energy. Let us then define the isotropic-equivalent energy in ejecta faster than u ,

$$E_{\text{iso}}(> u) = \int_u^\infty \frac{dE_{\text{iso}}}{du}(u') du', \quad (\text{B.1})$$

the isotropic-equivalent rest mass in ejecta faster than u ,

$$m_{\text{ej,iso}}(> u) = \int_u^\infty \frac{1}{c^2 \sqrt{1+u'^2}} \frac{dE_{\text{iso}}}{du}(u') du' \quad (\text{B.2})$$

(where c is the speed of light), and the isotropic-equivalent external medium mass swept by the blast wave when the four-velocity in its downstream is u ,

$$m_{\text{iso}}(u) = 4\pi r^3(u) n m_p / 3, \quad (\text{B.3})$$

where n is the number density of the external medium (assumed to consist of ionised hydrogen), m_p is the proton mass, and $r(u)$ is the distance travelled by the shock up to the time when its downstream four-velocity is u . Our energy conservation equation reads (cfr. Panaiteanu & Kumar 2000)

$$E_{\text{iso}}(> u) + m_{\text{iso}}(u)c^2 = \Gamma [m_{\text{ej,iso}}(> u) + m_{\text{iso}}(u)] c^2 + \Gamma_{\text{eff}} [(\Gamma - 1)m_{\text{iso}}(u)] c^2, \quad (\text{B.4})$$

where $\Gamma = \sqrt{1+u^2}$,

$$\Gamma_{\text{eff}} = \frac{\hat{\gamma}_{\text{ad}} \Gamma^2 - \hat{\gamma}_{\text{ad}} + 1}{\Gamma} \quad (\text{B.5})$$

is the ‘effective Lorentz factor’ that transforms the total internal energy from the fluid frame to the laboratory frame (Nava

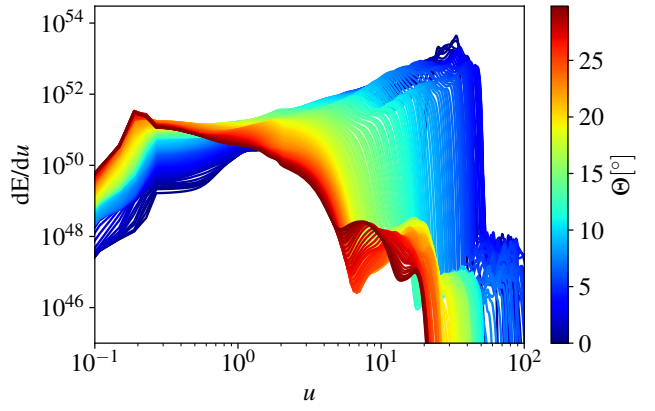


Fig. C.1: Velocity profile of the fiducial model for different polar angles.

et al. 2013), and $\hat{\gamma}_{\text{ad}}$ is the adiabatic index in the blastwave downstream, which we estimate following Pe'er (2012). The assumptions in this formulation are: (i) the ejecta faster than the blastwave downstream velocity u catch up immediately with it, injecting all their energy; (ii) the internal energy is dominated by that of freshly shocked external medium material (i.e. shocked over one adiabatic time scale, which corresponds roughly to one doubling in radius), which itself dominates in terms of mass over the material shocked at earlier time. Equation B.4 can be solved analytically for $m_{\text{iso}}(u)$, leading to

$$m_{\text{iso}}(u) = \frac{E_{\text{iso}}(> u)/c^2 - \Gamma(u)m_{\text{ej,iso}}(> u)}{[\Gamma(u) - 1][\Gamma_{\text{eff}}(u) + 1]}. \quad (\text{B.6})$$

The above equation establishes a one-to-one relation between $m_{\text{iso}}(u)$ and u , which can be turned into a relation between r and u using Eq. B.3, namely $r(u) = [3m_{\text{iso}}(u)/4\pi n m_p]^{1/3}$. The relation is monotonic and can be inverted numerically. This completely specifies the dynamics of the blastwave at each angular coordinate (Θ, Φ).

Appendix C: Light curves and fit results

In Figure C.2 we present the on-axis and off-axis light curves for all models, showing the effect of the jet's structural asymmetries, as discussed in Section 4.5.

Figures C.3 and C.4 present the corner plots resulting from the MCMC fitting procedure to the data of GW170817 using the axisymmetrised jet structures of the different models, as described in Section 4.6.

Figure C.5 presents the corner plots relative to the analogous MCMC fitting procedure using the non-axisymmetrised jet structure of model F and considering three different azimuthal viewing angles, as described in Section 4.5.

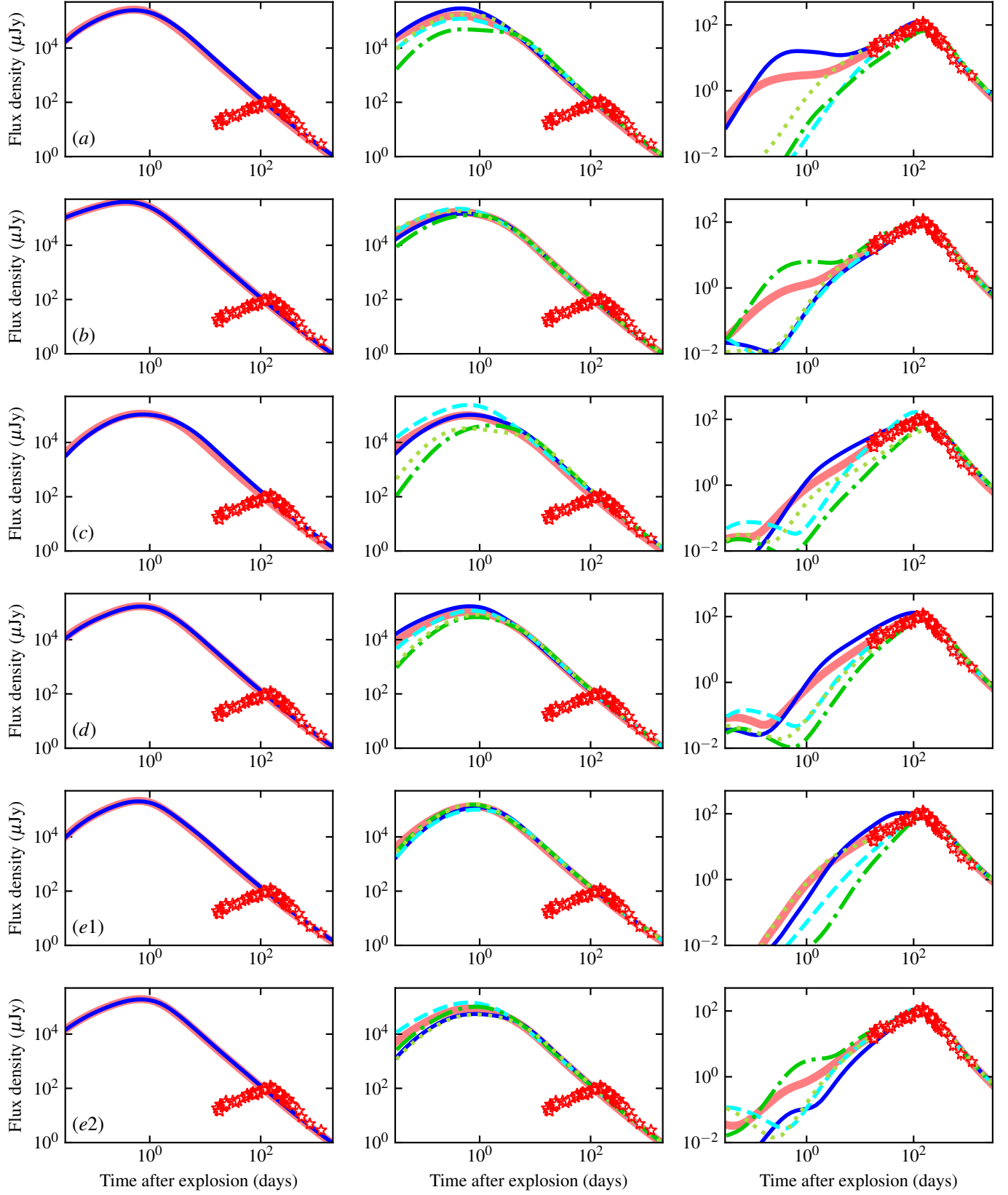


Fig. C.2: On-axis and off-axis light curves at 3 GHz comparing the axisymmetrised and non-axisymmetrised jet structures for all models, except for the fiducial one already presented in Section 4.5. Each row refers to a different model (indicated in the lower-left corner of the left panel), with the left, middle and right panels being the equivalent of Figs. 9, 10 and 11, respectively (also reflecting the same colours and line styles). For each model, the polar viewing angle θ_v in the rightmost panel is set to the best fit of that model, as reported in Table 2.

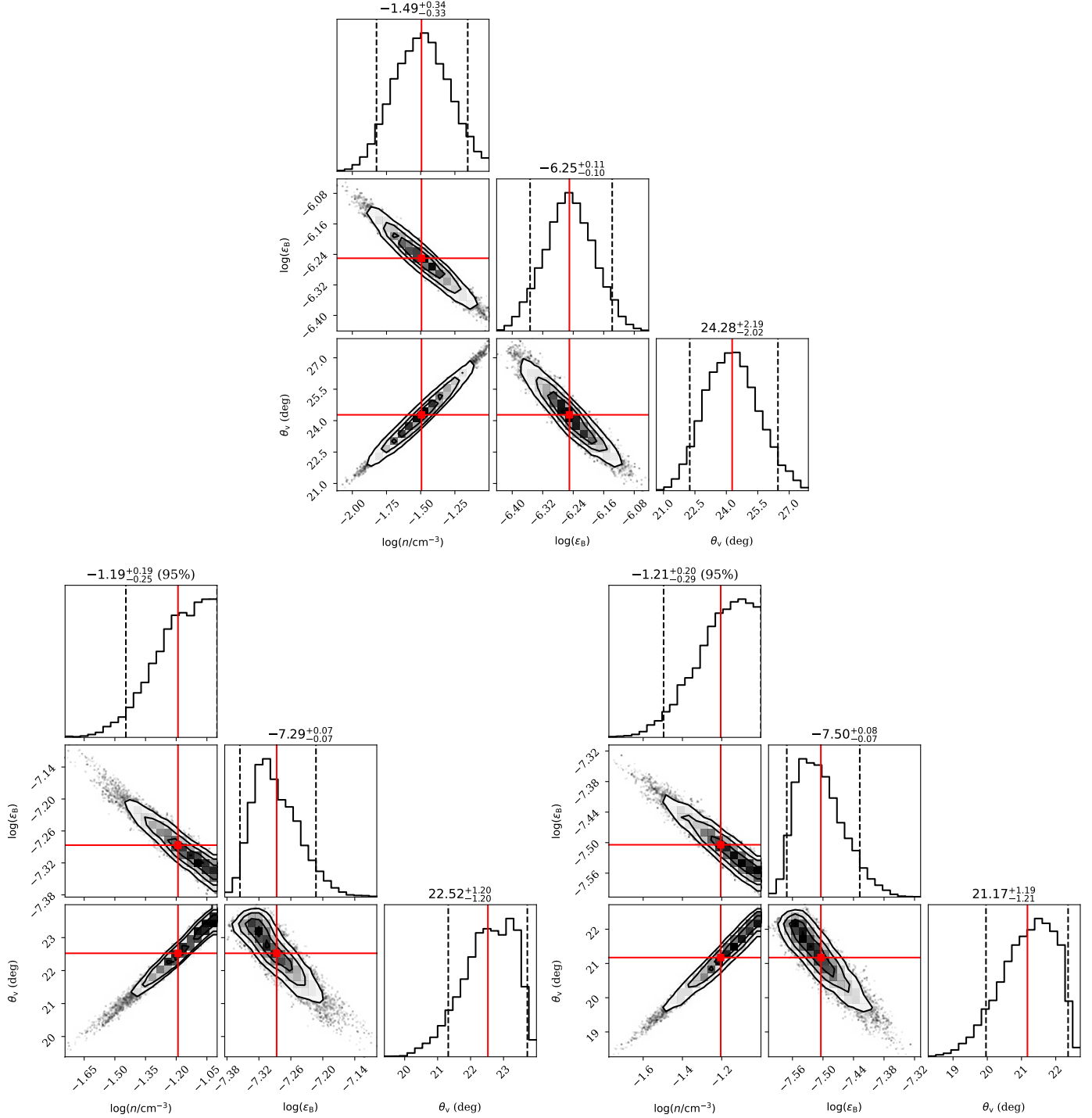


Fig. C.3: Corner plots of MCMC fit results of models *F*, *a*, and *b* to the GW170817 data. Each panel shows the marginalized one-dimensional (histograms) and two-dimensional (contours) posterior probability distributions of the parameters of the MCMC fit of the afterglow from a given jet model (*F*: upper panel; *a*: lower left; *b*: lower right). Vertical black dashed lines show the 5th and 95th percentiles of the one-dimensional posteriors, while red solid lines show the positions of the medians.

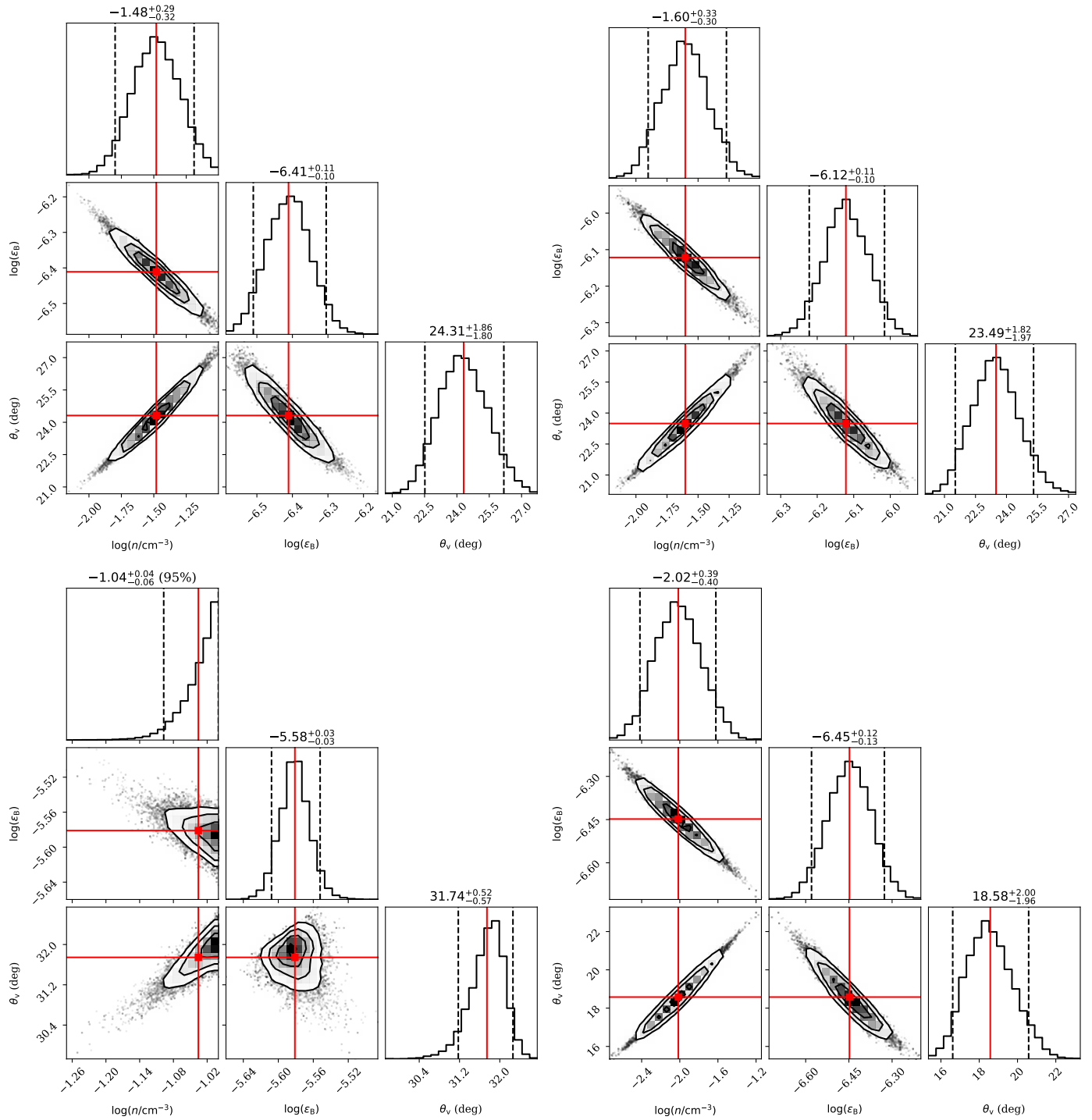


Fig. C.4: Corner plots of MCMC fit results of models *c*, *d*, *e1* and *e2* to the GW170817 data. Same as Fig. C.3, but for models *c* (upper left), *d* (upper right), *e1* (lower left) and *e2* (lower right).

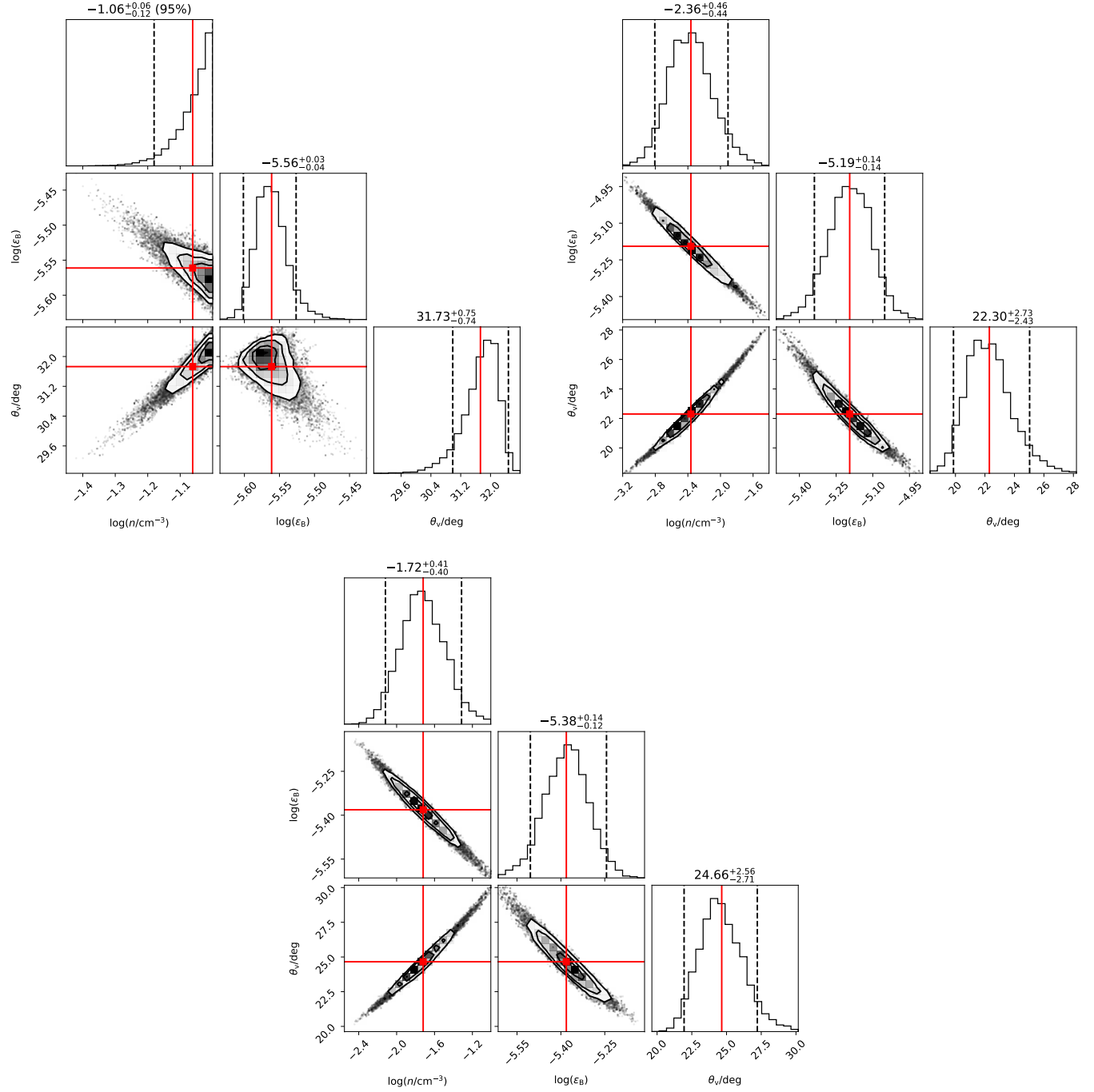


Fig. C.5: Corner plots of MCMC fit results of model *F* to the GW170817 data. Same as Fig. C.3, but considering the non-axisymmetrised jet structure and three different azimuthal viewing angles, i.e. $\phi_v = 0$ (upper left), $\phi_v = \pi/2$ (upper right), $\phi_v = \pi$ (bottom).